Available online at www.sciencedirect.com
ScienceDirect
International Journal of Heat and Mass Transfer 51 (2008) 4973–4984
International Journal of HEAT and MASS TRANSFER
www.elsevier.com/locate/ijhmt

Three-dimensional modelling of electric-arc development in a low-voltage circuit-breaker

L. Piqueras [a], D. Henry [a,*], D. Jeandel [a], J. Scott [a], J. Wild [b]

[a] *Laboratoire de Mécanique des Fluides et d'Acoustique, CNRS/Université de Lyon, École Centrale de Lyon/Université Lyon 1/INSA de Lyon, ECL, 36 avenue Guy de Collongue, 69134 Ecully Cedex, France*
[b] *Schneider Electric, 37 quai Merlin, 38050 Grenoble Cedex 9, France*

Received 30 August 2006; received in revised form 11 January 2008
Available online 21 April 2008

Abstract

This article describes direct numerical simulation of the first three milliseconds following ignition of the arc in a low-voltage circuit-breaker using a computational-fluid-dynamics code adapted for electric-arc modelling. The mobile electrode is allowed for by a moving mesh. The results describe the evolution of the arc with time in terms of its detailed electrical, thermal and fluid dynamic properties. They allow the identification of several phases during the overall arc development process studied here: arc initialisation in the widening electrode gap, arc-thermal expansion, displacement of the arc towards the tip of the mobile electrode, and the beginning of commutation to the fixed electrode.

PACS: 52.65.−y

1. Introduction

The low-voltage circuit-breaker is an important device for the safety of domestic electric circuits because it interrupts the current in the case of a short circuit. Fig. 1 illustrates the overall working of this device. An arc is established at contact opening and grows in extent. At a later time, coupled electromagnetic and gas dynamic effects cause the arc to jump (or commute) from the mobile electrode to a second fixed electrode before moving along the circuit-breaker between the fixed electrodes to enter the extinction chamber at the end of the circuit-breaker. There, the splitter plates cut the arc into small slices, thereby encouraging its extinction by cooling. The entire process of breaking the circuit takes only a few milliseconds.

In the development of such current breaking devices, it is important to understand as well as possible the arc dynamics and the physical processes occurring during circuit breaking. Many experimental studies have been published in the literature [1–7]. However, the extreme conditions and short time scales make measurements both difficult and very costly. In this context, despite the complexity of the phenomena which have to be taken into account, numerical simulation is an attractive approach which complements experimental measurements and provides information which it is often very difficult to obtain by other means.

In recent years, stimulated by the increasing performance of computers, many authors have worked on the numerical modelling of arcs in low-voltage circuit-breakers. Among them, Karetta and Lindmayer [8] developed a model of an arc between two parallel rails in a completely sealed chamber. The arc motion was studied, as were the distributions of electric potential, pressure and temperature in the arc chamber. The initial conditions were taken from a preliminary steady-arc calculation in which the magnetic force on the fluid was not allowed for. Subsequently, Lindmayer [9] carried out more detailed simulations of an arc moving along a divergent channel between two electrodes

* Corresponding author. Fax: +33 (0) 4 78 64 71 45.
E-mail address: daniel.henry@ec-lyon.fr (D. Henry).

0017-9310/$ - see front matter © 2008 Elsevier Ltd. All rights reserved.
doi:10.1016/j.ijheatmasstransfer.2008.02.035

Nomenclature

A	anode boundary
A	magnetic vector potential
B	magnetic field
c	sound speed
C	cathode boundary
E	exit section
E	total fluid energy per unit volume
I	total current
I_1	fraction of the current going through the moving electrode
I_2	fraction of the current going through the bottom rail
j	electric current density
k_T	thermal conductivity
M	mobile contact
p	pressure
P	plastic wall
S	symmetry plane
S_r	net radiation emission per unit volume
t	time
T	top boundary
T	temperature
v	velocity vector
W	right-hand wall
x	longitudinal horizontal coordinate
x_f	x coordinate of the front of the arc
x_h	x coordinate of the hottest point of the arc
x_r	x coordinate of the rear point of the arc
Xc	section plane perpendicular to the x-axis
y	vertical coordinate
Yc	section plane perpendicular to the y-axis
z	transverse horizontal coordinate
Zc	section plane perpendicular to the z-axis

Greek symbols

Δt	time step
Δx	smallest mesh size
μ	dynamic viscosity
μ_0	magnetic permeability of free space
ϕ	electric potential
ρ	fluid density
σ	electrical conductivity
$\bar{\bar{\sigma}}$	overall stress tensor
∇	nabla operator

under the influence of a transverse magnetic field. He also [10] studied the interaction of an arc with a splitter plate similar to that found in the extinction chamber of a circuit-breaker. Swierczynski et al. [11] developed a three-dimensional, unsteady model of an arc in a simplified low-voltage circuit-breaker geometry including the splitter plates. The distribution of electric current density at the electrode surfaces was imposed, with a prescribed procedure for determining the location of the centre of the distribution. The model predicts the arc motion due to the externally imposed magnetic field and shows the influence of the chemical composition of the gas on possible arc re-strike. Different behaviour as a function of the percentage of PA6 in a mixture with air resulted from dependence of the plasma physical properties on composition. In this context, Trépagnier, Martin, and Reggio [12] developed a more sophisticated model of plasma mixtures with multiple species, in which each species is described by a reaction–diffusion equation. They applied their model to study the influence of teflon vapour on the performance of circuit-breakers. A full two-dimensional model of circuit-breaker arcs suitable for arbitrary geometries has been developed by Schneider Electric (Chévrier et al. [13]). The resulting proprietary code allows two-dimensional simulation of the arc, from its birth between the fixed and mobile electrodes, to its disappearance between the extinction plates. In particular, this model has been used (Wild et al. [14]) to study and resolve a problem of re-strike in a circuit-breaker.

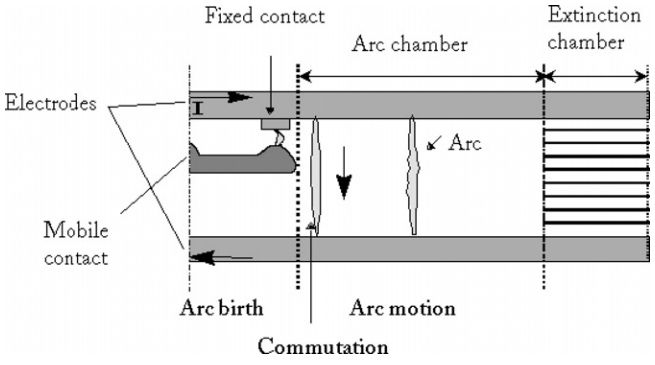

Fig. 1. Schematic diagram of the circuit-breaker showing the arc position at three different times.

This article describes three-dimensional modelling of the development of an electric-arc in a low-voltage circuit-breaker, a problem which has not, to our knowledge, been previously studied using numerical simulation. We first present the equations governing the arc dynamics and the numerical methods employed for the treatment of the arc problem. After presentation of the particular circuit-breaker geometry used in the study, we then give the simulation results. Detailed information concerning arc evolution (voltage, fluid-dynamics, energetics) is given, from the first stage of arc development until the beginning of commutation, representing a total period of 3 ms.

2. Electric-arc modelling and simulation

2.1. Electric-arc model

The electric-arc is a plasma consisting of ions, electrons and neutral particles. This gas mixture is assumed to satisfy the assumptions of local thermodynamic equilibrium and conservation of mass, momentum, and energy. It may be described by the Navier–Stokes equations, in which appear terms representing the electromagnetically induced force on the fluid, Joule heating and radiative cooling. The presence of these terms means we have to simultaneously solve equations for the electromagnetic part of the problem.

The fluid equations, including the additional terms, are

$$\frac{\partial \rho}{\partial t} + \nabla \cdot (\rho \mathbf{v}) = 0, \tag{1}$$

$$\frac{\partial \rho \mathbf{v}}{\partial t} + \nabla \cdot (\rho \mathbf{v} \cdot \mathbf{v}) = \nabla \cdot \bar{\bar{\sigma}} + \mathbf{j} \wedge \mathbf{B}, \tag{2}$$

$$\frac{\partial E}{\partial t} + \nabla \cdot (E\mathbf{v}) = (\mathbf{j} \wedge \mathbf{B}) \cdot \mathbf{v} + \nabla \cdot (\bar{\bar{\sigma}} \cdot \mathbf{v}) + \frac{\mathbf{j}^2}{\sigma} - S_r + \nabla \cdot (k_T \nabla T). \tag{3}$$

The unknowns, whose time evolution is described by these equations, are the density ρ, the momentum per unit volume $\rho\mathbf{v}$ ($\mathbf{v}$ being velocity), and the total fluid energy per unit volume E. The fluid pressure and viscous stresses are both contained in the overall stress tensor $\bar{\bar{\sigma}}$, while heat-conduction is governed by Fourier's law $k_T \nabla T$ (k_T is the thermal conductivity and T the temperature). Coupling to the electromagnetic field arises from the electromagnetic force $\mathbf{j} \wedge \mathbf{B}$ ($\mathbf{j}$ is the electric current density and $\mathbf{B}$ the magnetic field) and the Joule heating term $\mathbf{j}^2/\sigma$. Radiative cooling is represented by the net radiation emission per unit volume S_r.

The quantities $\mathbf{j}$ and $\mathbf{B}$ in the above equations are obtained by solving Maxwell's equations. Steady-state hypotheses have been adopted for the Maxwell equations, based on smallness of the dynamical time scales associated with the electromagnetic field compared with those of the fluid. Thus, at each time step in the solution of the Navier–Stokes equations, the electromagnetic field is determined instantaneously by the flow via the steady Maxwell equations. Further assuming no ferromagnetic materials, Maxwell's equations reduce to

$$\nabla \cdot (\sigma \nabla \phi) = 0, \tag{4}$$

$$\mathbf{j} = -\sigma \nabla \phi, \tag{5}$$

$$\nabla^2 \mathbf{A} = -\mu_0 \mathbf{j}, \tag{6}$$

$$\mathbf{B} = \nabla \wedge \mathbf{A}, \tag{7}$$

for the electric potential ϕ and magnetic vector potential $\mathbf{A}$ (σ is the electrical conductivity, not to be confused with the fluid stress tensor $\bar{\bar{\sigma}}$, and μ_0 is the magnetic permeability of free space).

Finally, thermodynamic data from CPAT at Toulouse [15] completed the model. These data take the form of tables of fluid density and internal energy, as well as viscosity, thermal and electrical conductivities, and radiative emission, as functions of pressure (0.5 bar, 1 bar, 2 bar, 4 bar, 8 bar, 16 bar) and temperature (from 300 K to 30,000 K). Rather than use the tables for $\rho(p,T)$ and $e(p,T)$ directly, because the Eqs. (1) and (3) describe the evolution of ρ and e, the original tables were interpolated and inverted to provide new tables for $p(\rho,e)$ and $T(\rho,e)$ which were used in the numerical scheme described below.

Boundary conditions, which are necessary to close the system, will be given in a next section.

2.2. Numerical methods

The original code is known as N3S-NATUR (developed by Simulog [16], in partnership with the French companies EDF, Renault and Snecma, and the laboratories of LMFA and INRIA) and solves the compressible Navier–Stokes equations for an ideal gas in three dimensions. It includes the option of a moving grid mesh, which allowed us to model the mobile electrode of the circuit-breaker. The mesh is nonstructured, composed of tetrahedra. Spatial discretisation is by a mixed P1 finite-element/finite-volume formulation in which the convective terms are treated by a finite-volume method, whereas the viscous, heat-conduction and source terms use a finite-element approach. The time-stepping scheme is explicit.

The arc plasma is not an ideal gas, requiring modification of the existing solver. The plasma properties are those of the tabulated data which replace the values used for an ideal gas. The numerical procedure for advancing by one time step has two stages:

(i) Solution of the discretised Navier–Stokes equations to obtain the quantities ρ, $\rho\mathbf{v}$ and E whose time evolution is directly described by these equations and from which ρ, $\mathbf{v}$ and e are determined;
(ii) T and p are then obtained from ρ and e by interpolation in the inverted tables $p(\rho,e)$ and $T(\rho,e)$, followed by direct use of the original tables to determine σ, k_T, μ, and $S_r(p,T)$.

The fact that the fluid is not an ideal gas also implies modification of the Roe scheme [17] (which implicitly supposed an ideal gas) used in the code to treat the convective flux terms. Calculation of the decentred fluxes of the dependent variables ρ, $\rho\mathbf{v}$ and E using Roe's procedure requires the Jacobian matrix of derivatives of these fluxes with respect to the dependent variables. Glaister [18] has proposed a procedure for calculating these derivatives in terms of the partial derivatives $\partial p/\partial e|_\rho$ and $\partial p/\partial \rho|_e$ and the dependent variables themselves. In the present study, we propose to determine the required derivatives by solving the system

$$c^2 = \frac{p}{\rho^2}\left(\frac{\partial p}{\partial e}\right)_\rho + \left(\frac{\partial p}{\partial \rho}\right)_e,$$

$$\Delta p = \left(\frac{\partial p}{\partial e}\right)_\rho \Delta e + \left(\frac{\partial p}{\partial \rho}\right)_e \Delta \rho,$$

where c is the sound speed (known from thermodynamic tables) and Δp, Δe and $\Delta \rho$ are the pressure, internal energy and density differences that arise in Roe's procedure. Simulations using the resulting numerical scheme for the test case of a shock tube containing a non-ideal gas can be found in [19].

The second modification of the solver is to incorporate the additional terms discussed earlier in the fluid equations and to solve for the electric potential and magnetic field. At each time step, the fluid part of the problem is solved first, allowing the electrical conductivity to be determined from the appropriate table. The electric potential equation is then solved using a finite-element scheme in the arc domain, defined as the region where the tabulated electrical conductivity is nonzero. The electrical conductivity in the plasma at mesh nodes on the electrode surfaces is taken equal to that of the electrode material, rather than having its tabulated value for the plasma. This method [20] has the effect of improved conservation of electric current and may also indirectly allow for the complex physical processes which occur in thin layers where the arc meets the electrode surface, layers which the solver does not treat directly. Boundary conditions for the electric potential are needed at the electrodes. Given linearity of the equation for ϕ, the potential difference is arbitrarily taken as 1 when solving this equation, $\phi = 1$ being imposed at the upper fixed electrode and $\phi = 0$ at the moving electrode and also at the lower fixed electrode when the arc reaches this electrode after commutation. The total electrical current under these conditions is then calculated by integration of the ohmic heating over the arc domain, as proposed by Wild et al. [14]. Finally, the solution is multiplied by an appropriate constant determined by the condition that the total electrical current through the arc have an externally prescribed value.

Given the electric potential, the current density is calculated and the equation for the magnetic vector potential solved by a finite-element method in the entire fluid domain. Boundary conditions are provided by a prior calculation of the magnetic potential at the boundaries using the Biot–Savart law, allowing for currents in the circuit external to the fluid region. To this end, the current distribution in the external domain is needed. This would, in principle, require the solution of a diffusion equation for the magnetic field within the metallic conductors, in particular the electrodes, coupled to the arc problem by boundary conditions at the electrode surfaces. The implementation of such an approach goes beyond the scope of the present work and we adopted a rather crude approximation in which the external current is taken to flow along a circuit of thin wires of prescribed form. One wire runs along the centreline of each electrode and carries the entire current of the electrode up to the point of maximum current density in the arc. Once the magnetic potential has been solved for within the arc, the magnetic field can be calculated. One then has all the information needed for determining the electromagnetic terms in the fluid equations at the next time step.

2.3. Circuit-breaker geometry

The simulation was performed on a double-breaking circuit-breaker developed by Schneider Electric [14]. This circuit-breaker has two symmetrical arc chambers. When a short circuit occurs, two arcs are created, one in each chamber. Although symmetry of the arcs will not be perfect(if only because of asymmetry in the wires carrying the current to/from the electrodes), for simplicity we assume perfect mirror symmetry and only consider half of the circuit-breaker, as shown in Fig. 2. The main dimensions of this geometry are 27 mm in length, 25 mm in height between the two fixed electrodes, and 6 mm in width. As our study is focused on the initiation of the arc, for simplicity sake, we have chosen not to model the splitter plates but to replace them by the wall denoted as W. The boundary conditions are summarized in Table 1. Symmetry conditions apply on the left-hand boundary denoted by S in Fig. 2. The other boundary conditions for ϕ and $\mathbf{A}$ have already been explained in the previous section. Those for temperature T on the electrodes are adiabatic conditions if $T < 3000$ K and a prescribed value of $T = 3000$ K otherwise, and for the other boundaries a prescribed value of $T = 300$ K. Finally, no-slip conditions are

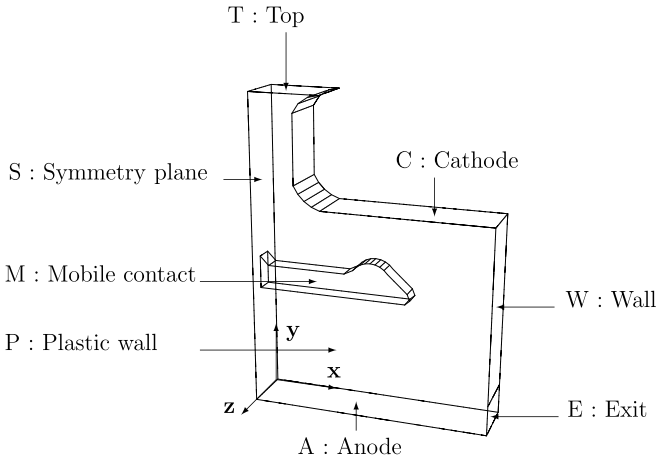

Fig. 2. Circuit-breaker geometry.

Table 1
Boundary conditions

	Symmetry plane, S	Contacts			Walls	Exit
		M	A	C	P W T	E
$\mathbf{v}$	$v_x = 0$	$v_x = v_z = 0$				
	$\frac{\partial v_y}{\partial n} = \frac{\partial v_z}{\partial n} = 0$	$v_y = -5$ m s^{-1}	$\mathbf{v} = 0$	$\mathbf{v} = 0$	$\mathbf{v} = 0$	–
T	$\frac{\partial T}{\partial n} = 0$	if $T < 3000$ K, $\frac{\partial T}{\partial n} = 0$; if not, $T = 3000$ K			300 K	–
p	–	–	–	–	–	1.3 bar
ϕ	$\frac{\partial \phi}{\partial n} = 0$	0	0	1	$\frac{\partial \phi}{\partial n} = 0$	$\frac{\partial \phi}{\partial n} = 0$
$\mathbf{A}$	$A_x = 0$					
	$\frac{\partial A_y}{\partial n} = \frac{\partial A_z}{\partial n} = 0$	Biot–Savart law				

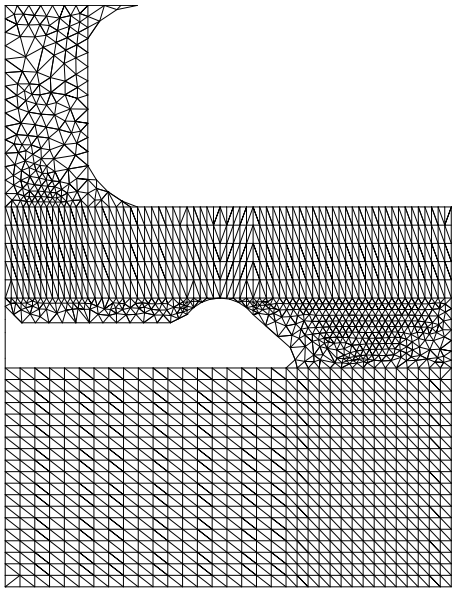

Fig. 3. Circuit-breaker mesh in the Zc plane at $t = 1$ ms.

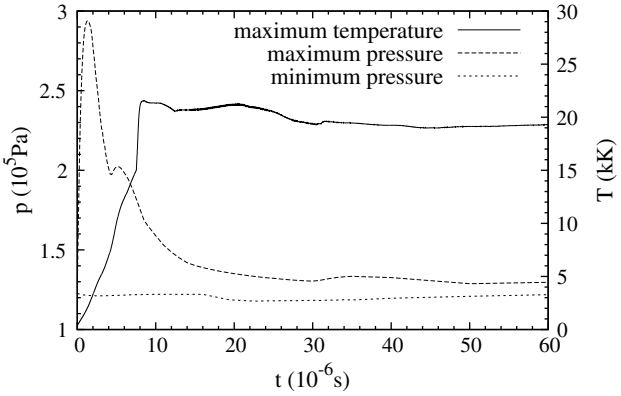

Fig. 4. Arc maximum temperature and minimum and maximum pressures as functions of time.

applied on all boundaries other than S, apart from a small section (denoted as E, 1 mm in height) at the bottom end of the right-hand boundary at which the pressure is imposed to be near atmospheric and equal to 1.3 bar. This is intended as a relatively crude representation of the outlet present at the base of the real circuit-breaker after the splitter plates.

For the sake of clarity in subsequent descriptions, we define three planes: Xc, Yc and Zc. Xc is a section across the circuit-breaker (perpendicular to the x-axis) through the highest point of the mobile electrode. Yc is parallel to the upper rail (perpendicular to the y-axis) and is equidistant from the upper rail and highest point of the mobile electrode. Finally, Zc is a centre plane (perpendicular to the z-axis).

The mesh used for the simulations has 118,026 tetrahedra and 22,930 nodes. Fig. 3 shows a two-dimensional slice through this mesh in the centre plane, Zc, of the circuit-breaker at $t = 1$ ms. The initial separation of the electrodes was taken as 0.5 mm. The mobile electrode moves downward at speed 5 m s^{-1}. Those mesh nodes which lie within the vertical extent of the mobile electrode have the same speed. The mesh within this region is moving, but does not deform with time. On the other hand, the mesh in a horizontal layer, bounded above by the fixed electrode and below by the top of the mobile one, is stretched vertically as time proceeds, while that below the mobile electrode is compressed.

3. Simulation results

The calculations were carried out on an Alpha Server HP 1280 GS. The time step Δt used varied between 10^{-8} and 5×10^{-8} s during the simulation. Such small values of Δt are imposed by the smallest mesh size Δx and the Courant Fredrichs Levy criterion. Δx is required to be small because of the moving-mesh: the mesh which is stretched needs to be initially small, whereas that which is compressed becomes smaller as time goes on. The CFL number, $c\Delta t/\Delta x$, took values between 0.16 and 0.88. Smallness of Δt in turn implies a relatively long computing time

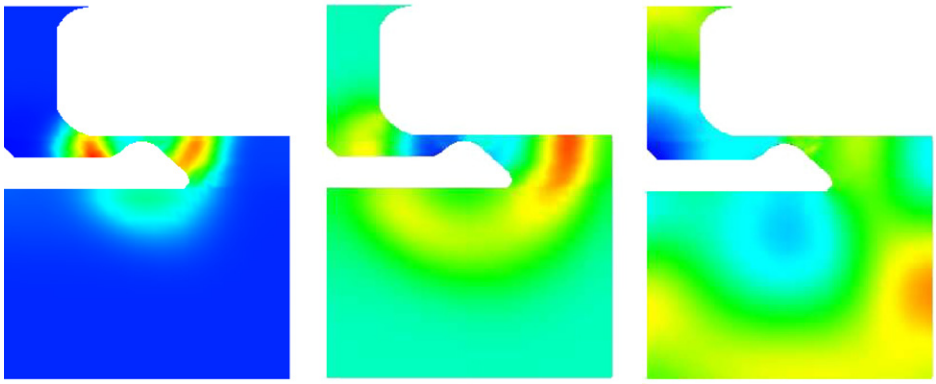

Fig. 5. Pressure field in the Zc plane at times $t = 14$ μs, $t = 26$ μs and $t = 56$ μs. The range of pressure values for each figure extends from the minimum to the maximum values shown in Fig. 4 at the given time.

to cover the arc evolution over several milliseconds. It took about 72 h of CPU to simulate 10^{-4} s of arc evolution. The breakdown of computing time was as follows:

- 47%: calculation of the electric potential,
- 23%: calculation of the magnetic field,
- 30%: Navier–Stokes solver.

This section of the paper describes results for the 3 ms of arc evolution which were simulated. We first examine arc initialisation, then the subsequent evolution of the arc is studied in terms of its electrical, thermal and fluid-dynamics properties up to the start of arc commutation. The results are presented using two-dimensional representations in three planes defined earlier.

3.1. Arc initialisation

The low-voltage circuit-breaker is calibrated so that, when the current exceeds a certain threshold value, the electrodes, which are initially in full contact, begin to separate. The electrode contact area decreases, leading to intense Joule heating as the current flow passes through microscopic roughness elements, melting the electrode surfaces and creating molten bridges of metal between the fixed and mobile electrodes. At larger separations, the molten bridges break, leading to the formation of an electric-arc in which the current is carried by a plasma.

To simulate arc birth, energy was injected into the initially cold gas (300 K, 1 bar) by introducing a source term on the right-hand side of the total energy Eq. (3). The source distribution had the form of a vertical cylinder located between the top of the mobile electrode and the upper fixed electrode. The source intensity had a Gaussian distribution of diameter 2 mm in the horizontal plane and a maximum value of 10^{12} W m^{-3} at its centre. Energy injection was continued until a temperature of 15,000 K was reached, which was found to occur after 6.4 μs with a total 10 J injected. At this temperature, the arc is capable of maintaining itself by Joule heating. Energy injection is then switched off and the arc allowed to evolve freely. The simulations show a very rapid rise in temperature followed by equilibration, while the pressure rises rapidly to a maximum and then falls (Fig. 4). Initialisation in the above artificial manner aims to replace the complex phenomena of melting, metallic-bridge formation and breaking described earlier and which give birth to the real arc. Given the relatively short time needed to equilibrate at arc temperatures, we hope and expect that, at the much longer times which are the object of this study, the arc will have forgotten the details of its birth.

An interesting feature of the arc initialisation is illustrated in Fig. 5, which shows the pressure field at three instants of time. A shock wave is produced, which rapidly expands and reverberates throughout the circuit-breaker volume. This behaviour in three dimensions may be contrasted with the two-dimensional results of Rachard et al. [21], in which essentially one-dimensional shock propagation led to strong effects when the shocks returned to the arc following reflection from the end walls. On the other hand, in the present case, the shocks do not strongly refocus back to the arc region and the maximum pressure falls relatively quickly, leading to near uniformity of the pressure within a short time (see Fig. 4).

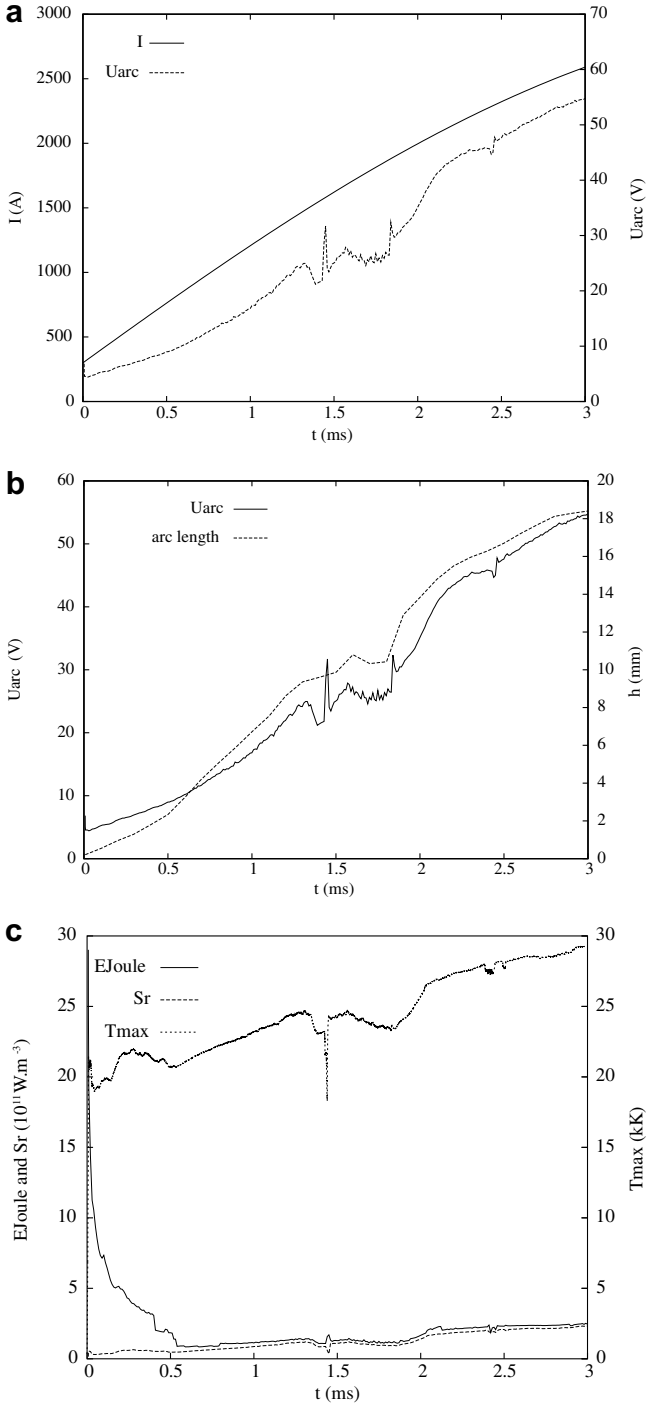

Fig. 6. Time evolution of the arc current and voltage (a), the arc voltage and length (b), Joule heating, *EJoule*, radiation loss, S_r, and temperature, T_{max}, at the hottest point in the arc (c).

The equilibrated temperature of around 22,000 K apparent in Fig. 4 is at the high end of experimental estimates of between 15,000 K and 20,000 K [1]. Our use of air as fluid, rather than a mixture of air and metallic vapour from the electrodes, may explain this. Moreover, the temperature is very sensitive to the model of radiation and the radiation data, and also to the heat losses at the electrodes. The simplified models used for radiation and at the electrodes may also influence the temperature variation. We should perhaps stress that, to our knowledge, although there is some experimental information, such as arc temperatures, no detailed measurements are available for comparison with simulations such as those described here.

3.2. Arc current and voltage

Fig. 6a shows the time evolution of arc current and voltage. The current is externally imposed and sinusoidal with a peak value of 3000 A and a frequency of 50 Hz. The contacts begin to open at a phase lag of 0.1 radians following zero current, corresponding to a time delay of 318 μs. This time of first contact opening corresponds to the beginning of the simulation and is taken as $t = 0$. The current at $t = 0$ is 299.5 A, rising to 2590 A by the end of the simulation at $t = 3$ ms. The arc voltage goes from 5 V to 54.8 V in the same period. Note that this is the potential difference across the arc itself and does not include the potential jumps at the electrode/arc interfaces (see e.g. Fiévet et al. [2] and Brdys et al. [6]). These jumps could be added in to the results to obtain the overall circuit-breaker voltage, but this does not affect the calculation itself since the current is imposed. Note also that the arc initialisation phase discussed in the previous subsection is of very short duration (about 10 μs) compared with the time period shown here.

The increasing arc length is known (Toumazet et al. [7], Lindmayer et al. [10]) to be closely correlated with the arc voltage. Fig. 6b shows the time evolution of arc voltage and length, the length being defined as the distance between the upper rail and the lowest point of the high-temperature (above 18,000 K) region corresponding to the arc. We observe a very close correlation between the two quantities.

3.3. Arc energetics

Fig. 6c shows the development with time of the rate of energy injection by Joule heating and the loss by radiation at the hottest point of the arc, as well as the temperature of

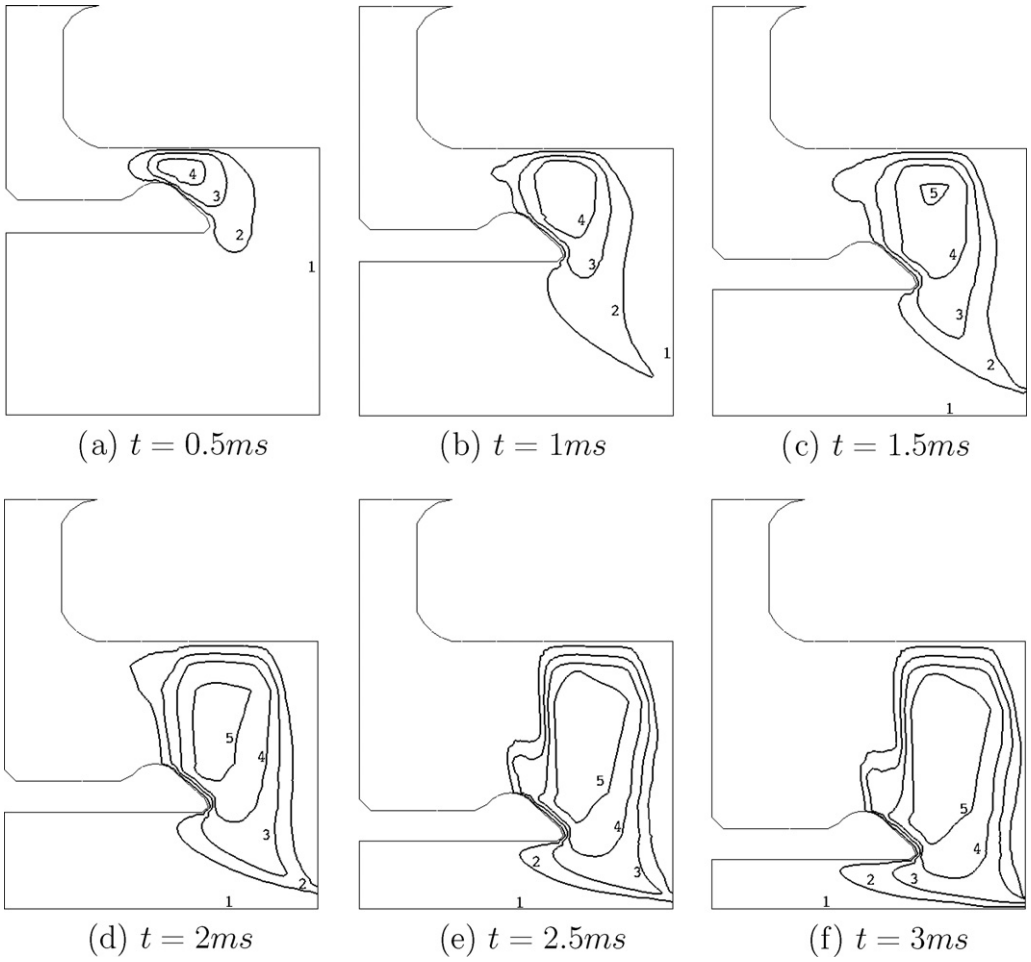

Fig. 7. Contours of constant temperature in the Zc plane (1: 300 K, 2: 6000 K, 3: 12,000 K, 4: 18,000 K, 5: 24,000 K) at different times.

this point. Initially, there is intense Joule heating due to the high current density in an arc of small diameter. Joule heating dominates radiation loss at this stage, but falls and becomes comparable with radiation loss for times beyond about $t = 0.6$ ms. The arc can then be considered as established with energy input by Joule heating slightly in excess of loss by radiation. Following arc establishment, the maximum temperature shows an overall slow rise from about 20,000 K to 29,000 K at $t = 3$ ms. This rise in temperature is associated with an increase in Joule heating. Also noticeable are two dips in temperature, which, as we shall see later, are related to fluctuations in the rear part of the arc.

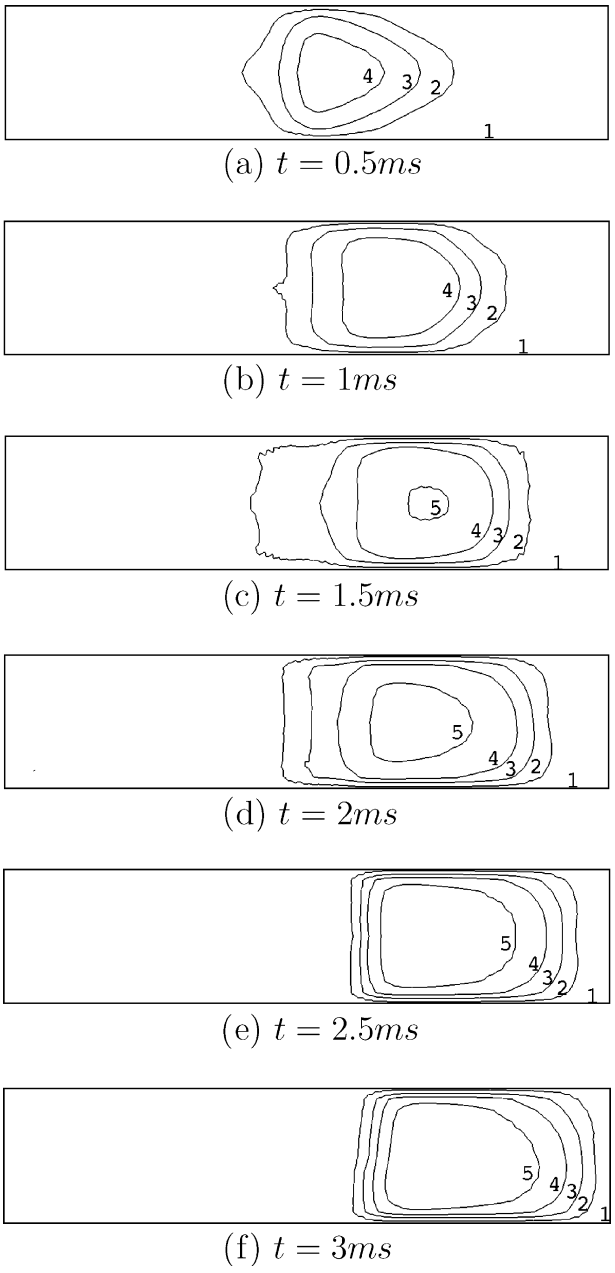

Fig. 8. Contours of constant temperature in the *Yc* plane (1: 300 K, 2: 6000 K, 3: 12,000 K, 4: 18,000 K, 5: 24,000 K) at different times.

3.4. Arc development

The increasing size of the arc and its motion (to the right) are apparent in Figs. 7 and 8, which show the fluid temperature at different times in the planes *Zc* and *Yc*. These figures also illustrate the evolution of the shape of the high-temperature zone corresponding to the arc.

To help further quantify the arc development, we calculated the x coordinate (recall the coordinate definition in Fig. 2) of the hottest point of the arc, as well as the front and rear, defined as the minimum and maximum values of x of the 18,000 K constant temperature contour. This representation (Fig. 9) illustrates both the arc motion towards increasing x and the variation in arc width. Fig. 10 provides another view in which the current density j is plotted along the line parallel to the x-axis formed by the intersection of planes *Yc* and *Zc* at a series of different times. The following discussion divides the arc development into a series of distinct phases.

During the first 0.5 ms, there is a phase of rapid thermal expansion. Fig. 10a allows an estimation of the arc expansion velocity of about 14.5 m s^{-1}. Fig. 9 provides further information: during this phase the front of the arc advances by 4 mm, whereas the hottest point only moves forward by 0.5 mm. There is thus some displacement, but faster growth in size of arc. This is also apparent in the behaviour of the rear point of the arc: according to Fig. 9, x_r actually decreases during part of this phase. Note that the phase of rapid expansion corresponds to that of dominance of Joule heating over radiation in Fig. 6c. Note also that, during this phase, the arc loses its initially circular form to become ovoid (see Fig. 8).

Between 0.5 ms and 1.35 ms, the arc advances rapidly towards increasing x. This is illustrated by Figs. 8a–c and 10b, while Fig. 9 provides further information. Firstly, at $t = 0.52$ ms, the x coordinate x_h of the hottest point abruptly advances by 1.2 mm. This rapid change appears

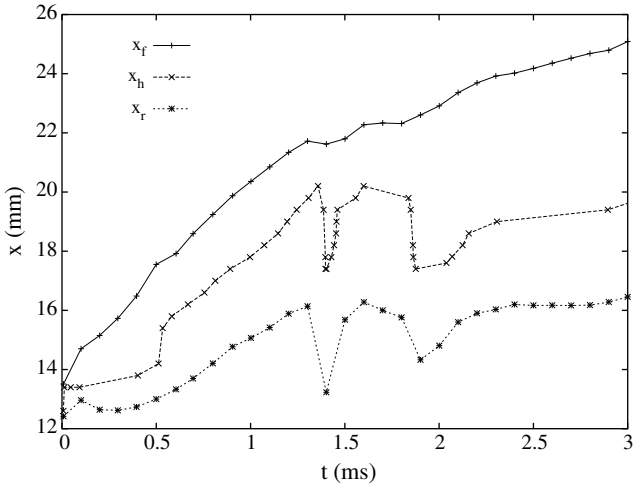

Fig. 9. Time evolution of the x coordinate of the hottest point (x_h), and of the front (x_f) and the rear (x_r) points of the arc.

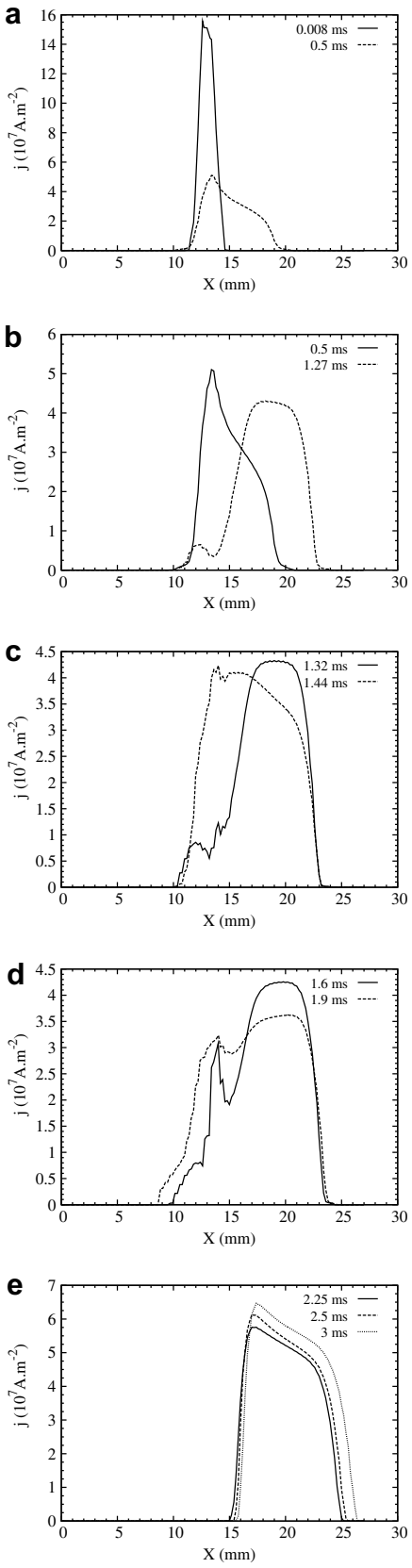

Fig. 10. Plots of the current density j along the line formed by the intersection of planes Yc and Zc at different times: (a) Phase of rapid thermal expansion, (b) phase of rapid arc displacement, (c) first fluctuation at rear of arc, (d) second fluctuation at rear of arc, (e) arc stabilisation.

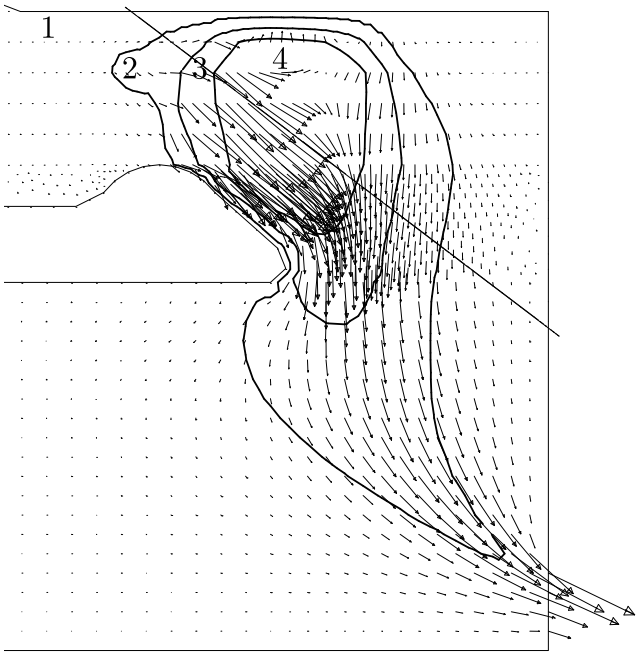

Fig. 11. Velocity and temperature fields in the Zc plane at $t = 1$ ms (temperature contours: 1: 300 K, 2: 6000 K, 3: 12,000 K, 4: 18,000 K). The oblique line defines a tranverse plane (parallel to the x-axis) used in Fig. 12.

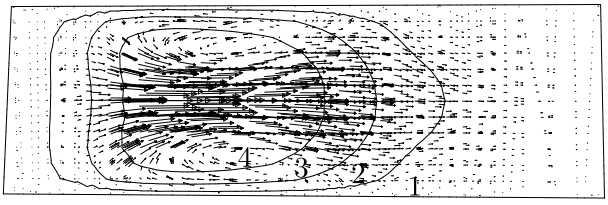

Fig. 12. Velocity and temperature fields in the transverse plane defined in Fig. 11 (temperature contours: 1: 300 K, 2: 6000 K, 3: 12,000 K, 4: 18,000 K). Note the presence of a vortex pair.

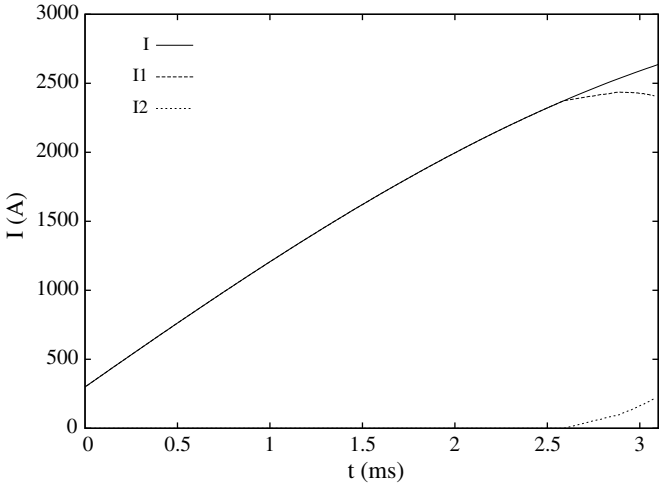

Fig. 13. Time evolution of the total current I and the two electrode currents I_1 (mobile electrode) and I_2 (bottom rail).

to correspond to the time when the foot of the arc leaves the top (largest y value) of the mobile electrode. Subsequently, the foot of the arc is attached to the diagonally slanting face of the moving electrode and the hottest point moves towards increasing x with a nearly constant velocity of 5.6 m s^{-1}. Both the front and rear of the arc essentially follow this trend.

In the next phase, between 1.35 ms and 2.25 ms, the front of the arc advances steadily at about 3.3 m s^{-1}, but we observe fluctuations at the arc rear, with backward jumps of both the hottest and rear points (Fig. 9). The first of these jumps occurs at $t = 1.4$ ms, while the second at $t = 1.8$ ms is preceeded by a more gradual backward displacement. Both of these fluctuations have similar characteristics: we note a drop in maximum temperature (Fig. 6c), a noticeable decrease in the arc voltage, followed by a peak (Fig. 6a), as well as the backward motion of the temperature maximum noted above (Fig. 9). These phenomena appear to be associated with the wake of hot electrically conducting gas which is left behind by the arc as it advances towards the right. This wake is apparent in the plots of current density at $t = 1.32$ ms and $t = 1.6$ ms of Fig. 10c and d. During fluctuation, the wake of conducting gas rises in temperature until it reaches arc temperatures and becomes just a rearward extension of the arc itself. This is reminiscent of the phenomenon of re-strike, in which a second arc forms behind the primary one during a phase of decreasing current. However, the fluctuations observed here, though they show similarities with re-strike, remain localised near the original arc and do not lead to a second one.

Following $t = 2.25$ ms, the arc width in the Yc plane stabilises at around 10 mm. From Fig. 10e, it appears the arc nonetheless continues to advance, a result which is borne out by the increase in the x coordinate of the arc front at the relatively low speed of 1.57 m s^{-1} according to Fig. 9. In this final phase, the arc appears to be strongly affected by the presence of the end wall of the circuit-breaker.

3.5. Flow fields

The development of the arc, and in particular its displacement, depends on the flow within the circuit-breaker. This flow is influenced by a number of factors: e.g. thermal expansion in the early stages of arc evolution, magnetic forces, outlet holes in the walls. Magnetic forces can be considered as having two sources: currents in the arc itself and currents in the electrodes. Both are of the same order of magnitude. The former ensures the coherence of the arc, while the latter strongly influences the arc displacement towards the end of the circuit-breaker.

The typical structure of the flow is illustrated by Fig. 11, which shows the velocity field in the Zc plane at $t = 1$ ms. At this time, the maximum velocity, attained inside the arc, is 442 m s^{-1}. The flow is principally directed towards the right and downwards. This is driven mainly by magnetic forces near and parallel to the diagonally slanting face of the mobile electrode and by the presence of the outlet hole at the bottom right.

Examination of the literature (Jones and Fang [22], Maecker and Stablein [23], Rachard et al. [21], Karetta and Lindmayer [8]) suggests the flow around a moving arc typically consists of two symmetrically located vortices on either side of the arc, as illustrated by Fig. 7 of Maecker and Stablein [23]. To observe this type of flow in our simulation, Fig. 12 shows the velocity field in an inclined transverse plane whose inclination was chosen to correspond with the dominant direction of velocity in Fig. 11. The results show that the flow is directed downwards and to the right within the arc core (due to the magnetic forces and outlet, as described above), but that there is a weaker

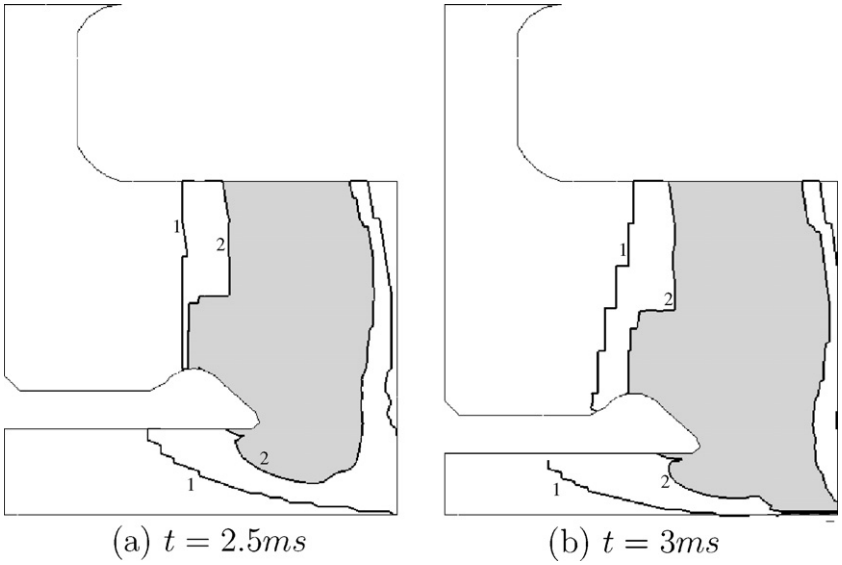

Fig. 14. Contours of current density in the Zc plane at $t = 2.5$ ms and $t = 3$ ms (contour values: 1: 0 A · m^{-2}, 2: 2 10^6 A · m^{-2}).

returnflow near the lateral walls. This flow indeed consists of two vortices of the type shown schematically in Fig. 7 of Maecker and Stablein [23].

3.6. Start of the commutation phase

Commutation refers to the transfer of the current carrying path (arc) from the mobile to the bottom fixed electrode. In the circuit-breaker, the total current I arrives via the upper rail. Prior to commutation, this current leaves via the moving electrode, while, following commutation, it leaves through the bottom rail. During commutation, a fraction I_1, goes through the moving electrode and the rest, I_2, goes through the bottom rail. Knowledge of either I_1 or I_2 enables quantification of the extent of commutation:

- Before commutation: $I_1 = I$, $I_2 = 0$,
- during commutation: $I = I_1 + I_2$, $I_1 \neq 0$, $I_2 \neq 0$,
- after commutation: $I = I_2$, $I_1 = 0$.

Fig. 13 shows the time evolution of I, I_1 and I_2 according to the simulation. I_2 becomes noticeably non-zero following $t = 2.6$ ms. Fig. 14 shows contours of current density at $t = 2.5$ ms and $t = 3$ ms in the Zc plane. At the second of these times, it is apparent from Fig. 14b that there are two current carrying paths: one leading to the mobile electrode (and present in Fig. 14a) and the other to the bottom rail.

The calculation was stopped at $t = 3$ ms because the maximum temperature exceeded 30,000 K, the highest value available in our thermodynamic tables. Nonetheless, it seems to us unlikely that the simulation would have led to complete commutation because the solid end wall of the simulated geometry constrains the arc too much for it to distance itself from the mobile electrode and detach completely.

4. Conclusion

A fluid-dynamics, moving-mesh simulation code has been modified to allow plasma-arc modelling. The code has been used to simulate the development up to the beginning of commutation of an arc in a three-dimensional geometry representing a low-voltage circuit-breaker. The results show several phases in the evolution of the arc. During the short initialisation phase, the temperature increases rapidly due to the intense energy input, before stabilising at around 20,000 K and beginning a second phase of strong thermal expansion. Next, there is a phase of arc displacement and increasing length: the arc, constrained by the walls, increases in length as the electrodes continue to separate, and moves towards the tip of the moving electrode at a velocity of order 5 m s^{-1}. Gas velocities within the arc are much larger and take the characteristic form of a vortex pair. The moving arc leaves behind a hot wake (between 6000 K and 10,000 K) which may sporadically undergo a sudden rise in temperature, producing a backwards jump of the rear boundary of the arc. Finally, after about 2.6 ms of the simulation, the commutation phase begins: an additional current carrying path to the bottom fixed electrode appears.

Acknowledgements

This work was supported by a fellowship cofunded by CNRS and Schneider Electric Company (L.P.).

References

[1] C. Fiévet, C. Fleurier, D. Hong, Temperature measurement in moving wall confined arcs, ICPIG XXI, Bochum, 1995.
[2] C. Fiévet, M. Barrault, P. Petit, P. Chévrier, C. Fleurier, V. André, Optical diagnostics and numerical modelling of arc re-strikes in low-voltage circuit-breakers, J. Phys. D: Appl. Phys. 30 (1997) 2991–2999.
[3] D. Hong, G. Sandolache, K. Lan, J.M. Bauchire, E. Le Menn, C. Fleurier, A radiation source developed for broad band optical absorption spectroscopy measurements, Plasma Sources Sci. Technol. 12 (2003) 1–7.
[4] D. Hong, G. Sandolache, J.M. Bauchire, F. Gentils, C. Fleurier, A new optical technique for investigations of low-voltage circuit-breakers, IEEE Trans. Plasma Sci. 33 (2005) 976–981.
[5] D. Cajal, A. Laurent, F. Gary, M. Mercier, S. Servant, A study of the various phases of the break in a low-voltage circuit-breaker thanks to the magnetic camera, J. Phys. D: Appl. Phys. 32 (1999) 1130–1135.
[6] C. Brdys, J.P. Touzamet, A. Laurent, J.L. Ponthenier, Optical and magnetic diagnostics of the electric arc dynamics in a low voltage circuit-breaker, Meas. Sci. Technol. 13 (2002) 1146–1153.
[7] J.P. Toumazet, C. Brdys, A. Laurent, J.L. Ponthenier, Combined use of an inverse method and a voltage measurement: estimation of the arc column volume and its variations, Meas. Sci. Technol. 16 (2005) 1525–1533.
[8] F. Karetta, M. Lindmayer, Simulation of the gasdynamic and electromagnetic processes in low voltage switching arcs, IEEE Trans. Compon. Pack. Manuf. Technol.-Part A 21 (1998) 96–103.
[9] M. Lindmayer, Complete simulation of moving arcs in low-voltage switchgear, in: 14th International Conference on Gas Discharges and their Applications, Liverpool, 2002.
[10] M. Lindmayer, E. Marzahn, A. Mutzke, T. Ruther, M. Springstubble, The process of arc-splitting between metal plates in low voltage arc chutes, in: 22nd International Conference on Electrical Contacts/ 50th IEEE Holm Conference on Electrical Contacts, Seattle, 2004.
[11] B. Swierczynski, J.J. Gonzalez, P. Teulet, P. Freton, A. Gleizes, Advances in low-voltage circuit-breaker modelling, J. Phys. D: Appl. Phys. 37 (2004) 595–609.
[12] J.Y. Trépanier, A. Martin, M. Reggio, Solution of multi-species gas flows in circuit-breakers with arc-wall interactions, in: 15th International Conference on Gas Discharges and their Applications, Toulouse, 2004.
[13] P. Chévrier, M. Barrault, C. Fiévet, J. Maftoul, J. Millon-Frémillon, Industrial applications of high-, medium- and low-voltage arc modelling, J. Phys. D: Appl. Phys. 30 (1997) 1346–1355.
[14] J. Wild, J.Y. Battandier, R. Delahaye, T. Devouassoux, M. Perrot, J.L. Ponthenier, 2D arc modelling of a double breaking circuit-breaker. Comparison with measurement and optimisation, in: 15th International Conference on Gas Discharges and their Applications, Toulouse, 2004.
[15] P. Teulet, A. Gleizes, private communication, 2003.
[16] D. Chargy, Manuel utilisateur N3S-NATUR V1.4 (in French) Simulog, 2002.
[17] P.L. Roe, Approximate Riemann solvers, parameter vectors, and difference schemes, J. Comp. Phys. 43 (1981) 357–372.
[18] P. Glaister, An efficient Riemann solver for unsteady flows with non-ideal gases, Comput. Math. Appl. 24 (1992) 77–93.

[19] L. Reynard, D. Henry, D. Jeandel, J. Scott, J. Wild, Towards three-dimensional modelling of electric arc initiation in a low-voltage circuit-breaker, J. High Temp. Mater. Process. 9 (2005) 555–570.
[20] J.J. Gonzalez, A. Gleizes, P. Proulx, M. Boulos, Mathematical modeling of a free-burning arc in the presence of metal vapour, J. Appl. Phys. 74 (1993) 3065–3070.
[21] H. Rachard, P. Chévrier, D. Henry, D. Jeandel, Numerical study of coupled electromagnetic and aerothermodynamic phenomena in circuit-breaker electric arc, Int. J. Heat Mass Transfer 42 (1999) 1723–1734.
[22] G.R. Jones, M.T.C. Fang, The physics of high power arcs, Rep. Prog. Phys. (1980).
[23] H.H. Maecker, H.G. Stablein, What keeps an arc standing in a cross flow? IEEE Trans. Plasma Sci. PS-14 (1986) 291–299.